Available online at www.sciencedirect.com
ScienceDirect
Trans. Nonferrous Met. Soc. China 32(2022) 2190−2204
Transactions of Nonferrous Metals Society of China
www.tnmsc.cn

Effects of extrusion temperature on microstructure evolution and mechanical properties of heterogeneous Mg−Gd alloy laminates via accumulated extrusion bonding

Shuai-shuai LIU[1,2], Han LIU[1,2], Bao-xuan ZHANG[1,2], Guang-sheng HUANG[1,2], Xiang CHEN[1,2], Ai-tao TANG[1,2], Bin JIANG[1,2], Fu-sheng PAN[1,2]

1. State Key Laboratory of Mechanical Transmission, College of Materials Science and Engineering, Chongqing University, Chongqing 400044, China;
2. National Engineering Research Center for Magnesium Alloys, Chongqing University, Chongqing 400044, China

Received 29 April 2021; accepted 18 December 2021

Abstract: The influence of extrusion temperature on microstructure and mechanical properties of heterogeneous Mg−1Gd/Mg−13Gd laminate prepared by accumulated extrusion bonding was investigated. The results reveal that the Mg−1Gd/Mg−13Gd laminate forms a significant difference in grain size between the successive layers when extruded at 330 °C, and this difference gradually disappears as the extrusion temperature increases from 380 to 430 °C. Besides, the growth rate of recrystallized grains in fine-grained layers is faster than that in coarse-grained layers. Moreover, the diffusion ability of Gd element increases with elevating extrusion temperatures, promoting the increase and coarsening of precipitates in fine-grained layers. Tensile tests indicate that the sample extruded at 380 °C has a superior combination of strength and ductility. This is mainly attributed to the synergy of the heterogeneous texture between coarse and fine-grained layers, hetero-deformation induced strengthening and hardening. The fine-grained layers facilitate the activation of prismatic ⟨*a*⟩ slips, while coarse-grained layers make it easier to active basal ⟨*a*⟩ and pyramidal ⟨*c*+*a*⟩ slips, especially for the sample extruded at 380 °C. The activation of pyramidal ⟨*c*+*a*⟩ slips contributes to coordinating further plastic deformation.

Key words: Mg−Gd alloys; heterogeneous structure; texture; mechanical properties; slip modes

1 Introduction

As the lightest metal material with a density of 1.8 g/cm^3, magnesium (Mg) alloys are attractive for potential applications in transportation, aerospace, military, communications, and electronic products owing to the advantages of high specific strength, vibrant damping capacity, and strong electro-magnetic shielding performance [1,2]. However, the activation of limited slip systems at room temperature leads to poor ductility and stretch formability, preventing the widespread application of Mg alloys [3]. Besides, traditional Mg alloys are difficult to achieve high strength and ductility, e.g., the tensile strength of high performance Mg alloys has reached greater than 500 MPa; however, the elongation is only about 5% [4]. The elongation of high-ductile Mg alloys can be more than 50%, but their tensile strength is usually less than 200 MPa [5]. Recently, the emergence of hetero-structure has provided us a new strategy to improve the strength and ductility of magnesium alloys simultaneously.

The heterogeneous structures have significant strength differences between soft and hard domains,

Corresponding author: Guang-sheng HUANG, E-mail: gshuang@cqu.edu.cn; Bin JIANG, E-mail: jiangbinrong@cqu.edu.cn
DOI: 10.1016/S1003-6326(22)65940-5

and the grain size changes from nanometer to micrometer [6], and they include gradient, heterogeneous lamellar, harmonic, bi-modal structures. During the tensile deformation, the mechanical incompatibility between domains generates significant hetero-deformation induced (HDI) stress with increasing strains [7]. This is owing to the fact that geometrically necessary dislocations (GNDs) accumulate at the interface to accommodate the strain gradient caused by the deformation incompatibility, which leads to extra strain hardening besides traditional dislocation hardening. The observed high strength is due to the HDI strengthening and enhanced ductility is attributed to the extra strain hardening, i.e., HDI hardening.

Extrusion and rolling processes can be used to effectively prepare heterogeneous structures. For instance, JUNG et al [8] prepared heterogeneous microstructure with fine grains (4.8 μm) and coarse grains (9.3 μm) in AZ80 alloy by aging prior to extrusion. WANG et al [9] fabricated a heterogeneous Mg−9Al−1Zn alloy with sub-micron and coarse grains by hard-plate rolling. GZYL et al [10] achieved a mixed grain structure in AZ31 alloy by equal channel angular pressing with low-temperature (150 °C). YAMASAKI et al [11] acquired a bimodal grain structure in Mg−Zn−Y alloy via the axisymmetric extrusion process. The studies above indicated that these materials with heterogeneous structures showed a superior combination of strength and ductility. They mainly focused on the process methods, while the effects of process parameters on the heterogeneous structure of Mg alloys are rarely studied.

Although the traditional rolling methodology has many advantages in the preparation of heterogeneous structures, edge cracks often occur during the rolling process due to the poor plasticity of Mg alloys, leading to the inefficient use of materials [9]. Therefore, a new technology of accumulative extrusion bonding (AEB) with a single pass deformation of 90% was developed as shown in Fig. 1, which effectively improved the plasticity of the alloy and avoided edge cracking [12]. Previous results showed that hetero-geneous Mg−1Gd/Mg−13Gd (wt.%) alloy laminate produced by the AEB exhibited outstanding strength−ductility synergy [13]. However, the effects of extrusion temperature on recrystallized grain size between different Gd content layers are still unclear. In order to regulate the heterogeneous structure and optimize the parameters of extrusion process, the effects of extrusion temperature on the microstructure evolution and mechanical properties of heterogeneous Mg−1Gd/Mg−13Gd laminates are systematically studied in this work.

2 Experimental

Two Mg−Gd binary alloys comprising 1 wt.% and 13 wt.% Gd were obtained by melting in an electric resistance furnace under the protection of a gas mixture of SF_6 and CO_2, then pouring into a steel mold preheated at 200 °C. The compositions of these ingots were measured to be Mg−0.98Gd (wt.%) and Mg−12.67Gd (wt.%) by inductively coupled plasma (ICP) spectrometry, respectively, which were very close to their respective nominal values. Subsequently, the Mg−1Gd and Mg−13Gd ingots were machined into the blocks with dimensions of 15 mm × 15 mm × 38 mm before

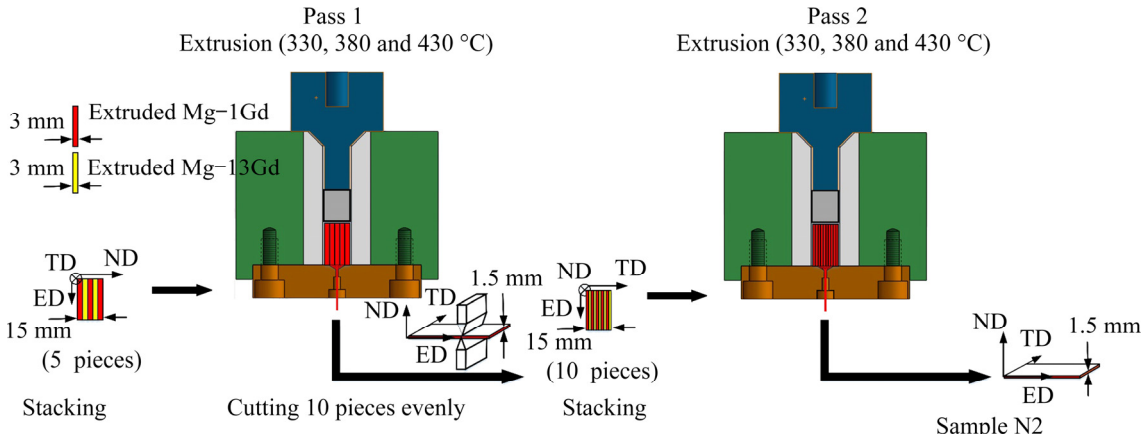

Fig. 1 Schematic diagrams of extrusion process for samples at different extrusion temperatures [12]

extrusion, and then homogenized at 500 °C for 24 h, followed by water quenching.

Figure 1 shows the preparation process of the samples at extrusion temperatures of 330, 380 and 430 °C via AEB. The blocks were extruded into sheets with the thickness of 3 mm at 380 °C as the starting material. The sheets were cut into the dimensions of 30 mm (extrusion direction, ED) × 15 mm (transverse direction, TD) × 3 mm (normal (thickness) direction, ND) from the initial sheet. The surfaces of these sheets were polished with a wire brush to remove the oxide layer, and then the polished sheets were degreased with alcohol. The treated 3 pieces of Mg−1Gd and 2 pieces of Mg−13Gd were stacked alternately and extruded into sheets with the thickness of 1.5 mm at different temperatures, which was denoted as 1-pass sample. Then, 10 pieces of 1-pass sample were stacked and extruded into sheets with the thickness of 1.5 mm at above three temperatures, which was denoted as 2-pass sample (hereafter referred to as Sample N2). The samples were indirectly extruded at a plunger speed of 6 mm/s, and the extrusion ratio was 12.8.

The microstructures were observed via optical microscope (OM), field-emission scanning electron microscope (SEM, JOEL JSM 7800F) equipped with an HKL electron backscatter diffraction (EBSD) detector. The EBSD characterization was operated at 20 kV, 15 mm working distance, 70° tilt, and with 1 μm scan steps. The analysis of EBSD data was performed by HKL Channel 5 analysis software. The uniaxial tension tests along ED were carried out on an universal testing machine (CMT6305−300KN) with a strain rate of 1×10^{-3} s^{-1} at room temperature. The dog-bone shaped specimens for tension have a gauge size of 18 mm × 6 mm along ED. The tensile tests for each sample were repeated three times to acquire reliable results.

3 Results

3.1 Microstructure and texture evolution

Figures 2(a−c) show the microstructures of Sample N2 on the ED−ND plane at different extrusion temperatures. As indicated by arrows in Fig. 2(a), the alternately distributed dark black and bright white layers represent fine-grained layers Mg−13Gd and coarse-grained layers Mg−1Gd, respectively. The bonding interfaces are clearly visible and form a relatively good bonding quality without delamination after extrusion. Meanwhile, the laminate thickness is uneven, which might be due to the differences in flow stress across the constituent layers. The large friction between the extrusion container and the die is also one of the

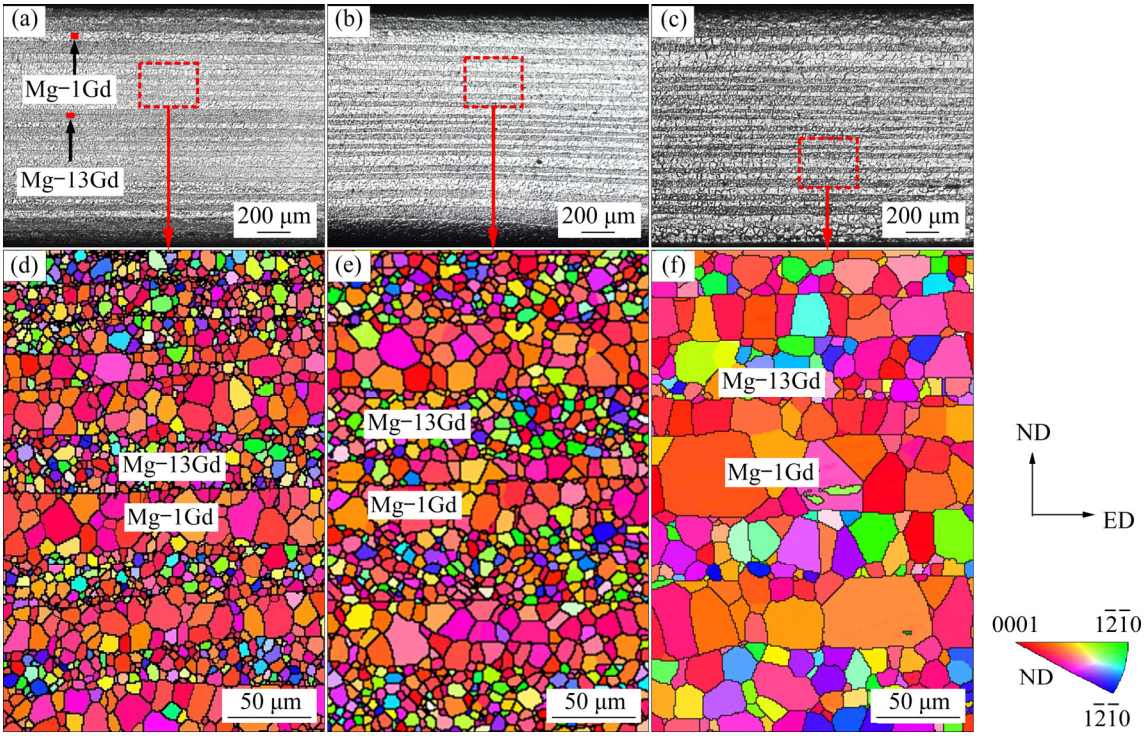

Fig. 2 Optical micrographs (a−c) and corresponding IPFs (d−f) in optical micrographs marked by dotted boxes of Sample N2 at different extrusion temperatures: (a, d) 330 °C; (b, e) 380 °C; (c, f) 430 °C

reasons for the uneven laminate thickness. Figures 2(d−f) are the corresponding inverse pole figures (IPFs) marked by dotted boxes in Figs. 2(a−c). The results show that grains in all layers have undergone complete recrystallization. Interestingly, Sample N2 at 330 and 380 °C exhibits significantly different grain sizes in alternating layers. Furthermore, coarse-grained and fine-grained sizes hardly change with increasing extrusion temperature. As the temperature increases to 430 °C, it is observed that grains of coarse-grained and fine-grained layers have grown up distinctly, which is similar to the homogeneous structure. Some grains in fine-grained layers are even close to the layer thickness along ND.

Figure 3 shows {0001} pole figures of Sample N2 at different extrusion temperatures. The prior literature vastly reported that rolled or extruded Mg alloy plate generally exhibited a basal texture and the {0001} poles tilted from ND towards RD or ED slightly [14,15]. In present study, a double-peak basal texture (Figs. 3(a, b)) is formed in coarse-grained layers of Sample N2 after extrusion at 330 and 380 °C. It inclines the basal poles ±30° from ND towards ED (Fig. 3(d)). This may be due to the activation of pyramidal ⟨*c*+*a*⟩ slip systems [16−18], which is also confirmed by the in-grain misorientation axes (IGMA) distribution. The micro-texture reveals that coarse-grained layers at 330 °C exhibit a texture intensity of 14.33, which is above twice that in fine-grained layers (7.14). When extrusion temperature increases to 380 °C, a similar texture component is remained and the texture intensity values of coarse-grained and fine-grained layers are slightly reduced to 14.91 and 7.76, respectively.

Herein, for coarse-grained layers, it is worth noting that the texture feature of Sample N2 at 430 °C is different from the double-peak basal textures formed at 330 and 380 °C. Previous literature showed that the double-peak basal texture was generated mainly by the enhanced activity of pyramidal ⟨*c*+*a*⟩ slips and its backward crystal rotation toward the {0001} pole during the relaxation [19]. The larger recrystallized grain size for Sample N2 at 430 °C makes the critical resolved shear stress (CRSS) of non-basal slip systems much higher than that of its counterparts at 330 and 380 °C, resulting in the activation of few slip systems [17]. KOIKE et al [20] also indicated that the CRSS of non-basal slip systems increased with increasing grain size. However, it was reported that the CRSS of pyramidal ⟨*c*+*a*⟩ slips significantly decreased when the deformation temperature increased [21,22]. Therefore, the CRSS of pyramidal ⟨*c*+*a*⟩ slips at 430 °C may exist a competitive relationship between the extrusion temperature and the grain size. Compared with the

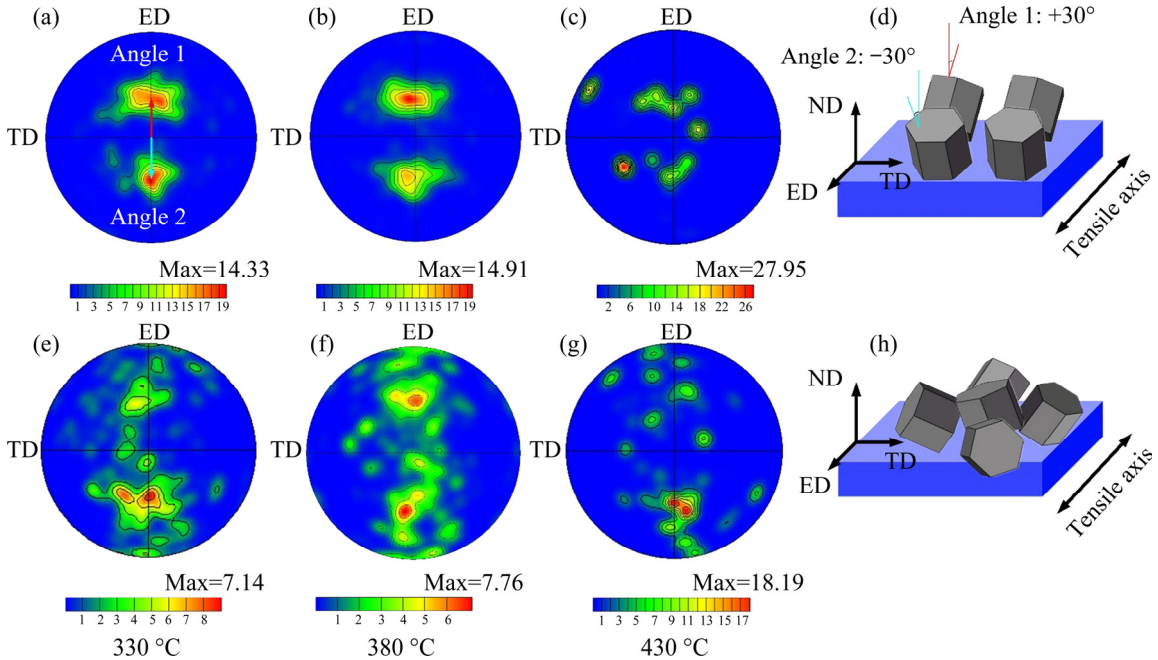

Fig. 3 Texture evolution of {0001} pole figures of Sample N2 in coarse-grained (a−c) and fine-grained (e−g) layers from IPFs of Fig. 2, and diagrams of crystal deflection in coarse-grained (d) and fine-grained (h) layers

texture feature of Sample N2 at 330 and 380 °C, the effect of grain size on the CRSS of pyramidal ⟨*c*+*a*⟩ slips at 430 °C is dominant and the activity of pyramidal ⟨*c*+*a*⟩ slips decreases, resulting in the disappearance of the double-peak basal texture.

From the perspective of fine-grained layers, the *c*-axes of Sample N2 at 330 and 380 °C deflect different angles along ED and disperse toward TD (Figs. 3(e, f, h)). This is mainly due to the fact that the Gd solute clusters within matrix and Gd segregation at GBs can act as effective obstacles to hamper the motion of dislocations and GBs, which greatly influences the recrystallization behavior and promotes the texture to be distributed randomly during hot deformation [23]. In addition, the texture distribution in fine-grained layer of Sample N2 at 430 °C (Fig. 3(g)) is similar to that of Sample N2 at 330 and 380 °C.

Table 1 shows the average grain sizes (AGSs) of coarse-grained and fine-grained layers in Sample N2 at different extrusion temperatures. It was reported that the DRXed grain size (d_{DRX}) after hot deformation was closely related to the Zener−Hollomon value (Z) [24], as shown in Eqs. (1) and (2):

$$Z=\dot{\varepsilon}\exp[Q/(RT)] \tag{1}$$

where $\dot{\varepsilon}$ is the strain rate, Q is the lattice diffusion activation energy, R is the molar gas constant, and T is the deformation temperature. The relationship between d_{DRX} and the Z value can be expressed as [25]

$$Zd_{DRX}^{m}=A \tag{2}$$

where m is the grain size exponent and A is a constant. It can be seen from Eqs. (1) and (2) that the Z value and d_{DRX} are governed by only two parameters (strain rate and deformation temperature) [12]. The extrusion rate in this work is constant, so the extrusion temperature is the only factor affecting the d_{DRX}. At 330 °C, the AGSs of coarse-grained and fine-grained layers are 8.8 and 4.6 μm, respectively. With the increase of extrusion temperature, the AGSs of coarse-grained and fine-grained layers gradually increase. Particularly, the AGSs of coarse-grained and fine-grained layers sharply increase to 13.6 and 11.2 μm at 430 °C, respectively, which accords with Eqs. (1) and (2). In order to quantitatively study the growth rate of coarse-grained and fine-grained layers at different extrusion temperatures, it can be further deduced the relationship between AGS (d) and parameter Z according to Eqs. (1) and (2) as follows:

$$\ln d=k\ln Z+b \tag{3}$$

where k and b are constants. Based on the AGSs of coarse-grained and fine-grained layers as well as the extrusion temperature, Fig. 4 reveals the $\ln d$−$\ln Z$ curves and fitting results of linear relationship.

Table 1 AGSs of coarse-grained and fine-grained layers in Sample N2 at 330, 380 and 430 °C

Temperature/°C	Size of coarse-grained layer/μm	Size of fine-grained layer/μm
330	8.8	4.6
380	10.9	5.8
430	13.6	11.2

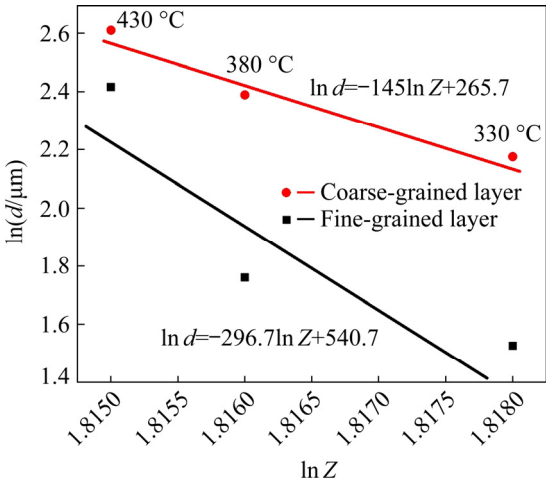

Fig. 4 Relationship of grain size d and parameter Z of Sample N2 at different extrusion temperatures

According to the slope of linear relationship, the growth rate of fine-grained layers is much higher than that of coarse-grained layers with increasing extrusion temperature, which is related to the movement of grain boundaries (GBs). It is well known that the grain growth is actually the process of grain boundary migration. The relationship among the movement speed (v) of GBs, the driving force (p) for GB migration and the radius (r) of curvature is as shown in Eqs. (4) and (5) [25]:

$$v=m_1p \tag{4}$$

$$p=\gamma(1/r_1+1/r_2) \tag{5}$$

where m_1 is the proportional constant, representing the mobility of GBs, γ is the GBs energy, and r_1 and

r_2 are the radii of curvature of two adjacent grains, respectively. Although more precipitates in fine-grained layers have a certain hindering effect on the GB movement, the driving force for GB migration of fine-grained layers is higher than that of coarse-grained layers, resulting in higher movement speed of GBs in fine-grained layers. Therefore, the growth rate of fine-grained layers is much faster than that of coarse-grained layers, which is consistent with the experimental results.

Figures 5(a−c) show the SEM images of Sample N2 at different extrusion temperatures. The enlarged SEM images (Figs. 5(d−f)) clearly indicate that a large number of fine precipitates locate in fine-grained layers, distributing at GBs and within grain interiors, whereas a few particles are detected in coarse-grained layers. This is because a solid-solution state can be maintained in Mg−1Gd layers with a lower Gd content, while the higher Gd content in the Mg−13Gd layers exceeds the limit of solid solubility, so that precipitates are formed during extrusion deformation [13]. As shown in Figs. 5(g−i), the EDS point scanning was conducted on the precipitates of Sample N2 at different temperatures. The results show that they are mainly Mg_5Gd and Mg_3Gd, which are similar to the results of KIM et al [13]. Meanwhile, the precipitates in fine-grained layers gradually increase and coarsen with increasing temperature. Moreover, some particles even reach ~6.7 μm at 430 °C. This is attributed to the fact that the probability of the atom gaining energy to exceed the barrier increases, improving the atomic diffusion capacity at the elevated temperatures [26].

This can be further supported by an Arrhenius equation that the diffusion coefficient of Gd in Mg (D_{Gd}) is calculated as follows [27]:

$$D=9.8\times10^{-6}\exp[-127804/(RT)] \quad (6)$$

In this study, the holding time is 15 min. The D_{Gd} values of Sample N2 at 330, 380 and 430 °C are 8.2×10^{-17}, 5.86×10^{-16} and 3.1×10^{-15} m^2/s by Eq. (6), respectively. The corresponding root mean square (RMS) diffusion distance is 0.27, 0.72 and 1.67 μm. Utilizing the EDS area scanning results in Fig. 6, the superimposed maps of Mg (marked by

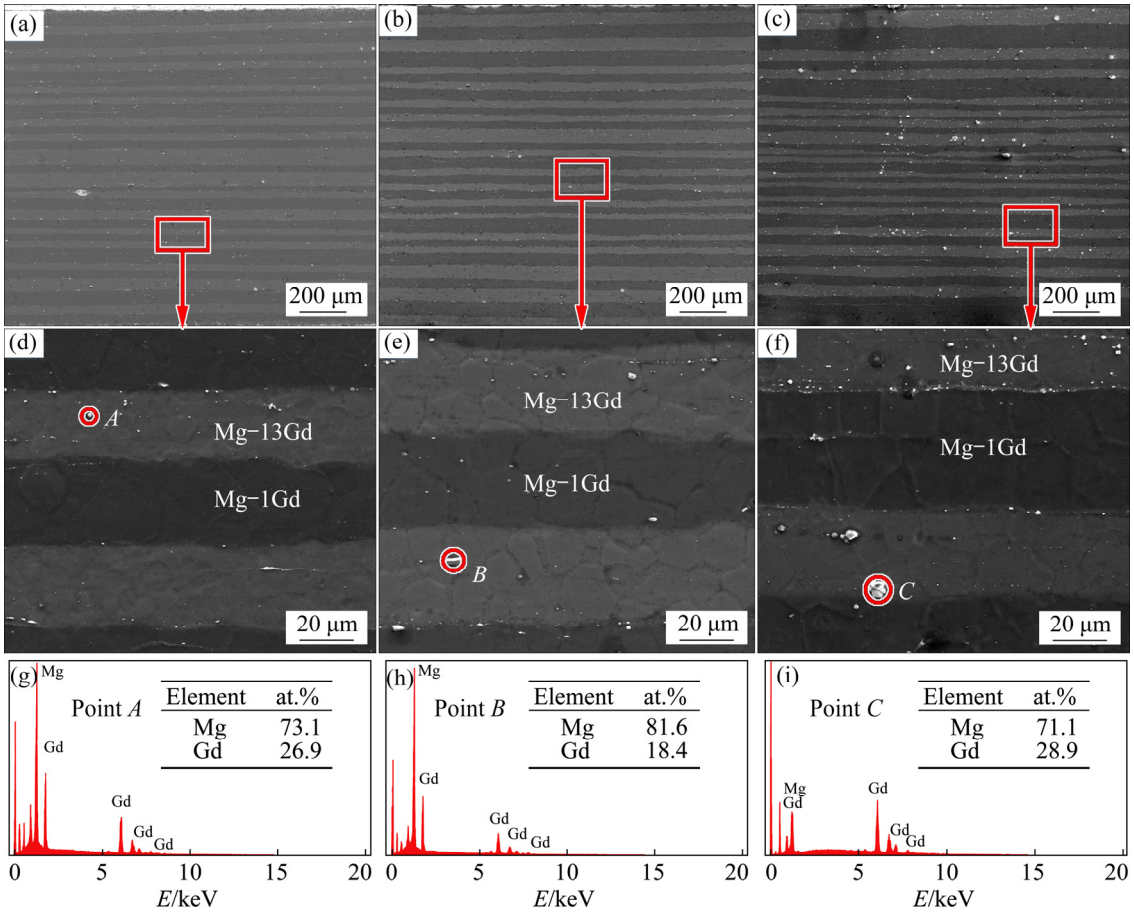

Fig. 5 SEM images of Sample N2 at 330 °C (a, d), 380 °C (b, e) and 430 °C (c, f), and corresponding EDS point scanning results of Points *A*, *B* and *C*, respectively (g−i)

red) and Gd (marked by green) elements visually exhibit the distribution of Gd and Mg elements in coarse-grained and fine-grained layers. Obvious contrast of Mg−Gd particles is consistent with the distribution of precipitates and the point scanning EDS results. Note that there is no obvious bulk diffusion at different extrusion temperatures because the RMS diffusion distance is far less than the layer thickness. However, the RMS diffusion distance gradually increases, which indicates that the diffusion ability of Gd element increases with increasing extrusion temperature.

3.2 Mechanical properties

Figures 7(a) and (b) display the true stress−true strain curves and the variation trend of tensile properties of Sample N2 at different extrusion temperatures. The results of tensile properties are summarized in Table 2. The ultimate tensile strength (UTS) and elongation (EL) of Sample N2 both increase firstly and then decrease with increasing extrusion temperature. The changing trend of EL is more obvious, while the yield strength (YS) shows a slight decrease with increasing extrusion temperature. It is well known that grain size is an important factor affecting the mechanical properties of metals. Based on the Hall−Petch law, the smaller grain size contributes to improving YS of extruded alloys at room temperature. This is the main reason why Sample N2 at 330 °C has the highest YS, whereas its EL is inferior to that of the sample at 380 °C. Besides, the poor bonding between different component layers induces the propagation of fracture along layer interfaces during tensile tests, resulting in lower EL of Sample N2 at 330 °C. The tensile fracture morphology in Fig. 8(a) also confirms that.

At 380 °C, Sample N2 exhibits an optimal balance of strength and ductility (YS (144.5±6.3) MPa, UTS (291.0±7.8) MPa and EL (20.6±1.4)%). In addition to the grain refinement and precipitate strengthening, the synergy between coarse- and fine-grained layers, HDI strengthening and hardening are responsible for the improvement of mechanical properties. However, Sample N2 at 430 °C has the lowest strength and ductility, which is different from the research results of HU et al [28]. They found that the sample with coarse

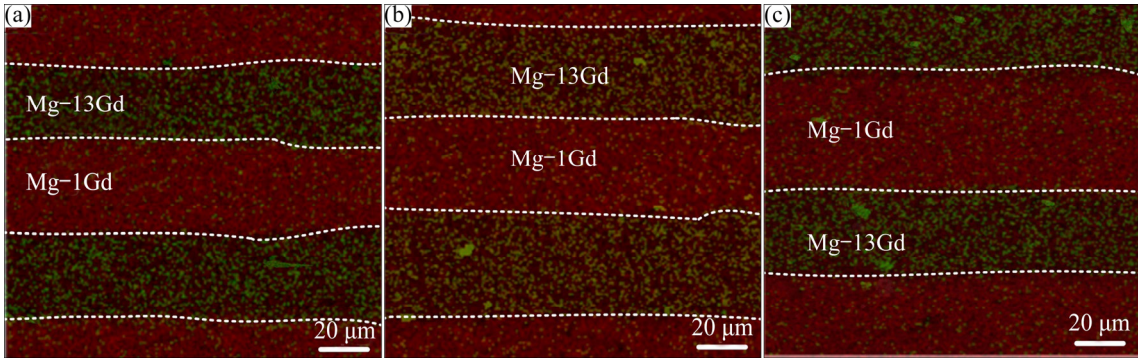

Fig. 6 Superimposed EDS area scanning mappings (a−c) of Mg (marked by red) and Gd (marked by green) elements corresponding to Figs. 5(d−f)

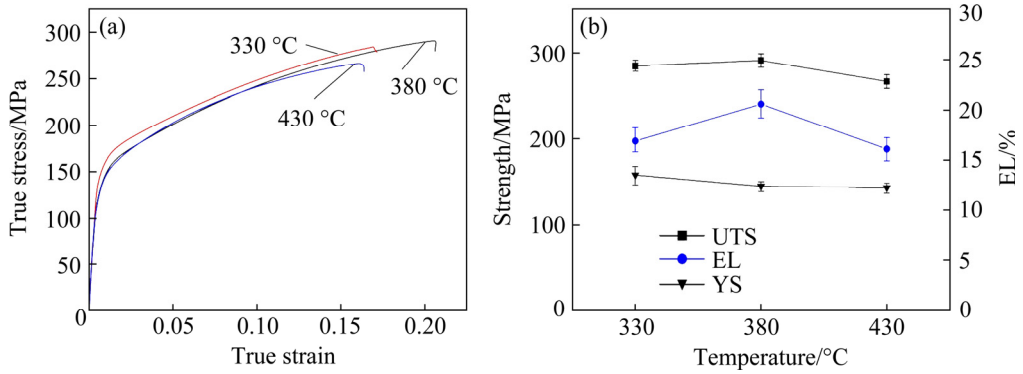

Fig. 7 True stress−strain curves of Sample N2 at different extrusion temperatures (a) and corresponding variation trend of tensile properties (b)

Table 2 Tensile properties of Sample N2 at different extrusion temperatures

Temperature/°C	YS/MPa	UTS/MPa	EL/%
330	157.8±7.5	284.5±6.7	16.9±1.5
380	144.5±6.3	291.0±7.8	20.6±1.4
430	142.7±9.2	266.4±8.3	16.1±1.1

grains exhibited a decrease of strength and an increase of elongation at high temperatures. There are three main reasons for the phenomenon in this work. Firstly, more coarse precipitates hinder the movement of dislocations and GBs, resulting in stress concentration, which makes these precipitates become crack sources. Secondly, the GBs and layer interfaces provide a path for crack propagation. Thirdly, excessive coarsening of grains induces the generation of brittle fracture regions and decreases the strength.

3.3 Fracture morphology

The SEM images of fracture surfaces of two magnifications of Sample N2 at different extrusion temperatures are shown in Fig. 8. It is clearly that the sample presents severe separation phenomenon of layer interfaces at 330 °C after fracture, while the constituent layers of Sample N2 at 380 and 430 °C are still well bonded. According to the fracture morphology characteristic, the layer interfaces of the Mg−13Gd and Mg−1Gd can be easily distinguished as marked by the dashed lines in Figs. 8(d−f). These precipitates as the crack sources are detected at the bottoms of the dimples at different extrusion temperatures. A large number of particles are also found at the interface of Sample N2 at 330 °C. The Mg−1Gd layers show a typical ductile fracture, which is characterized by dimples, while the fracture surfaces of the Mg−13Gd layers

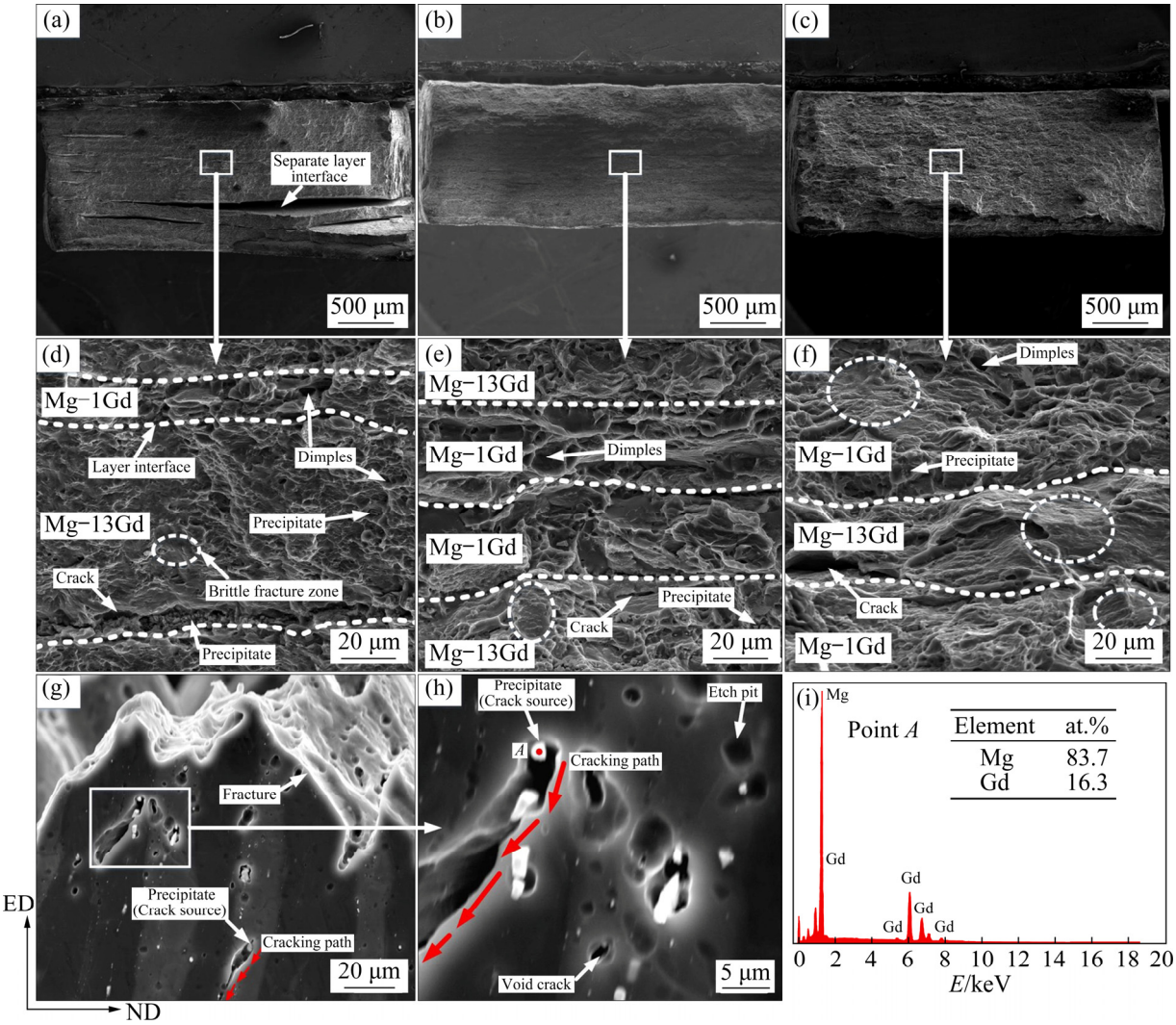

Fig. 8 SEM morphologies of fracture surfaces of Sample N2 at 330 °C (a, d), 380 °C (b, e), and 430 °C (c, f), SEM morphologies of Sample N2 at 430 °C near fracture (g, h), and EDS point scanning results (i) of Point *A* in (h)

are a mixture of small and shallow dimples, as well as brittle fracture zones. Compared to Sample N2 at 330 °C, it is observed that Sample N2 at 380 °C shows larger dimples in Mg−1Gd layers, indicating the improvement of ductility. However, for Sample N2 at 430 °C, the number of brittle fracture zones in the Mg−13Gd layers increases. Some brittle fracture zones even appear in Mg−1Gd layers, which is associated with coarse precipitates. Moreover, these particles identified as Mg−Gd phase (Fig. 8(i)) cause crack initiation and propagation, which induces the appearance of brittle fracture zones as shown in Figs. 8(g, h), thus resulting in the decrease of ductility [29].

4 Discussion

4.1 Mechanism for improvement of strength and ductility

It is reported that basal slips can be activated easily at room temperature due to the low CRSS, while the Schmid factor (SF) values related to texture have a significant effect on basal slips [30]. Thus, based on the obtained EBSD data and {0001} pole figures (Fig. 3), the SF maps for basal slips and corresponding histogram distributions of coarse-grained and fine-grained layers were calculated. The results are shown in Fig. 9.

The double-peak basal textures of coarse-grained layers in Sample N2 at 330 and 380 °C are located in soft orientation regions (Figs. 9(a, b)). The deflection of grained *c*-axis towards ED in coarse-grained layers helps for the activation of basal slips when the tensile direction is along ED. The texture component of fine-grained layers spreads along ED of SF maps (Figs. 9(d−f)), which contributes to the activation of basal and non-basal slips [9]. Thus, coarse-grained layers maintain strong work hardening ability, while fine-grained layers not only provide strength, but also coordinate

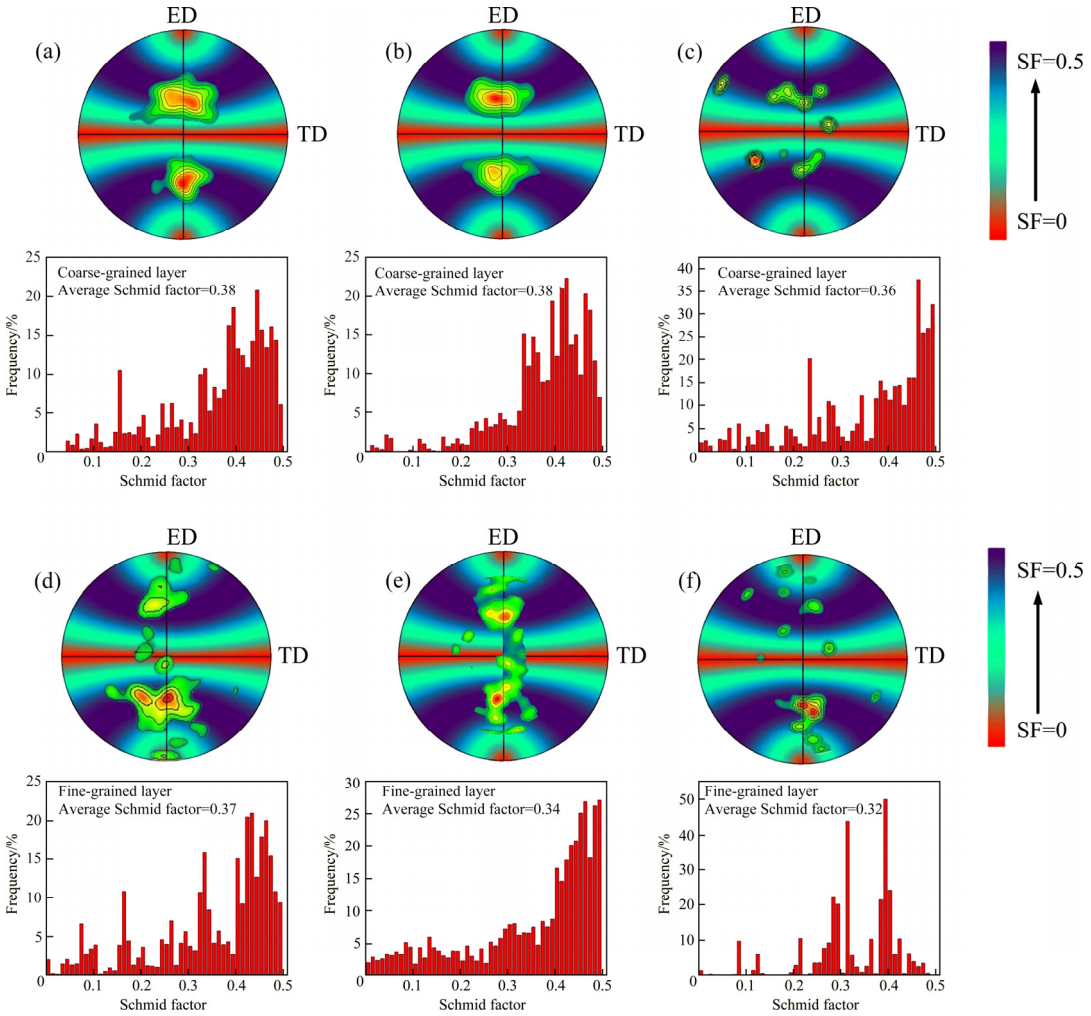

Fig. 9 SF maps for basal slips in {0001} pole figures and corresponding histogram distributions of coarse-grained and fine-grained layers at different extrusion temperatures: (a, d) 330 °C; (b, e) 380 °C; (c, f) 430 °C

plastic deformation. Sample N2 at 330 and 380 °C possesses similar texture feature and SF distribution. Meanwhile, the distribution of their precipitates has no obvious difference based on Figs. 5(d, e). These results lead to a small difference in strength and ductility. However, Sample N2 at 380 °C presents excellent ductility without sacrificing strength. It is necessary to consider the effect of HDI strengthening and hardening on mechanical properties.

Based on our previous study about the heterogeneous Mg−Gd alloy laminates [31], when coarse-grained and fine-grained layers co-deform elastically, the plastic strain caused by dislocation slips firstly occurs in coarse-grained layers during the heterogeneous deformation process. However, coarse-grained layers cannot deform freely because of the constraint by fine-grained layers, generating the strain gradient near the interface in coarse-grained layers, which needs GNDs to accommodate the strain gradient. Consequently, the accumulation of GNDs at the interface in coarse-grained layers leads to the formation of long-range back stress. In terms of physical process, the back stress will give rise to the generation of forward stress along the opposite direction. The interaction of back stress and forward stress makes the generation of HDI stress. To remain continuity of strain, the samples need to overcome HDI stress, thereby exhibiting HDI strengthening [31,32]. The coarse-grained layers undergo higher plastic deformation with increasing strain, which stimulates more GNDs to accommodate the increasing strain gradient, resulting in HDI hardening [33]. In summary, the back stress makes the soft domain stronger and the forward stress makes the hard domain weaker if it is deformable [7].

In order to evaluate the effect of HDI strengthening and hardening at different extrusion temperatures, the loading−unloading−reloading (LUR) tests of Sample N2 were performed. The results are shown in Fig. 10(a). It can be seen from Fig. 10(b) that three samples show obvious

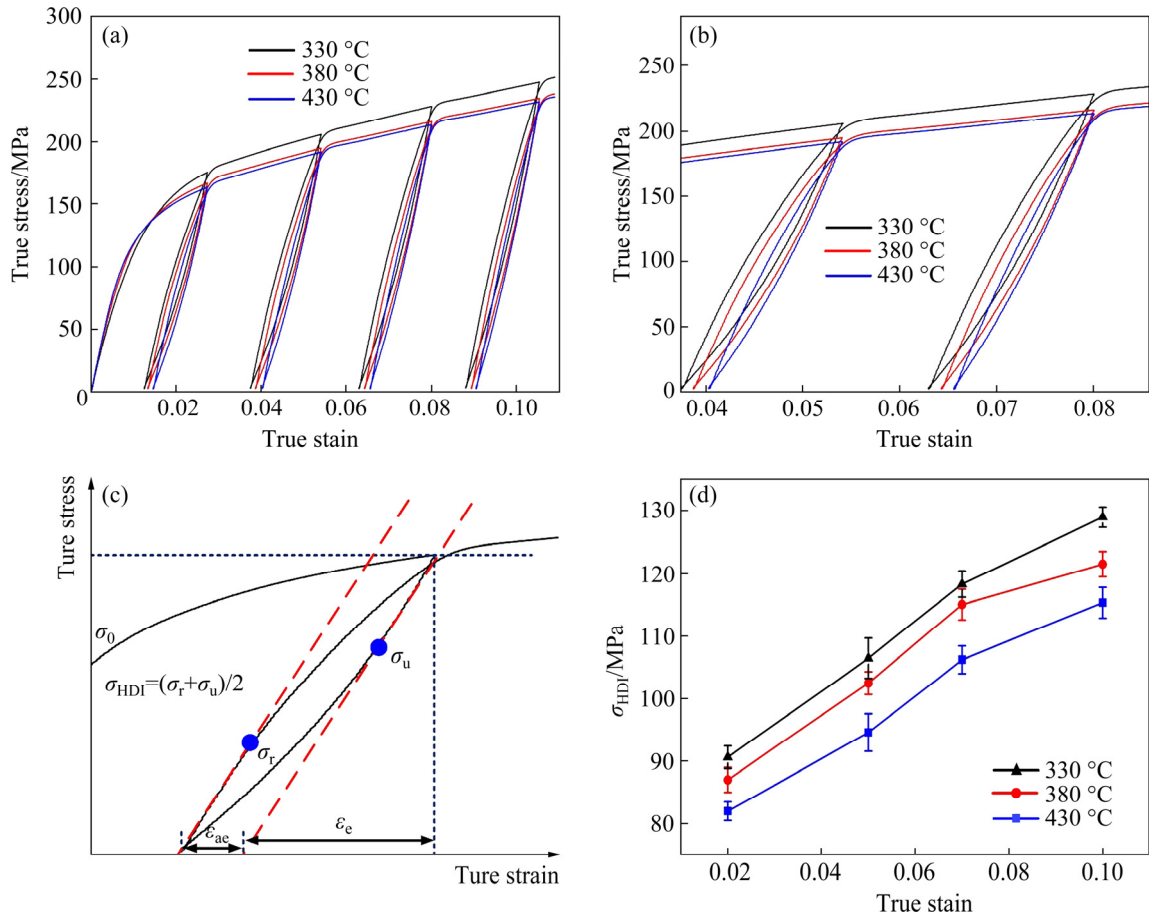

Fig. 10 LUR tensile curves of Sample N2 at 330, 380 and 430 °C (a), partially enlarged hysteresis loops of different samples (b), calculated schematic diagram of HDI stress (ε_{ae} and ε_e represent anelastic recovery strain and elastic recovery strain, respectively) (c), and evolution of HDI stress with true strain (d)

hysteresis loops, especially for Sample N2 at 330 °C, which indicates that this sample has the most significant Bauschinger effect and inhomogeneous deformation. This is related not only to the heterogeneous structure, but also to the texture and grain boundary of Mg alloys [34]. The HDI stress is calculated by Eq. (7) [35]:

$$\sigma_{HDI}=(\sigma_u+\sigma_r)/2 \quad (7)$$

where σ_u and σ_r represent the unloading and reloading yield stress, respectively, as shown in Fig. 10(c). The calculated results demonstrate that the HDI stress of Sample N2 at 380 °C is ~121.5 MPa under 10% strain, which contributes to ~52.6% of the flow stress. Although Sample N2 at 330 °C has the highest HDI stress, its poor bonding interface is not conducive to the HDI strengthening and hardening effect at later deformation. Therefore, Sample N2 at 380 °C has the optimal HDI strengthening and hardening effect, which plays a significant role in improving the strength and ductility.

Besides, the formation of twins also plays an important role in coordinating plastic deformation. The obvious twinning modes in Mg alloys are tensile twins $\{10\bar{1}2\}\langle\bar{1}011\rangle$ and compression twins $\{10\bar{1}1\}\langle\bar{1}012\rangle$, which are produced by tension and compression along the *c*-axis of grains or compression and tension perpendicular to the *c*-axis of grains, respectively [36]. Among various twins, the CRSS of the tensile twin is the lowest. Therefore, the plastic deformation of basal slips and tensile twins may occur simultaneously in Mg alloys. The band contrast (BC) maps of three samples after tensile tests are presented in Figs. 11(a−c). Some twins are observed at three samples, especially for coarse-grained layers of Sample N2 at 430 °C. This is attributed to the fact that coarse-grained layers have larger dislocation slip range [37]. Moreover, the serious stress concentration near the grain boundary is easy for twins to nucleate. However, the dislocation slip range is smaller in fine-grained layers, and the local stress concentration can be released by cross slips, non-basal slips, grain boundary sliding and dynamic recovery so that the stress conditions cannot meet the requirement of twin nucleation [37]. BARNETT et al [38] suggested that the dominant deformation modes of Mg alloys changed from $\{10\bar{1}2\}$ tensile twins to slips at room temperature when the grain size decreased to a certain extent. Therefore, it is easier to activate tension twins in coarse-grained layers. This can be also confirmed from the orientation angle distribution of the samples in Figs. 11(d−f), where the coarse-grained layers have higher proportion in the misorientation range of 85°−88°.

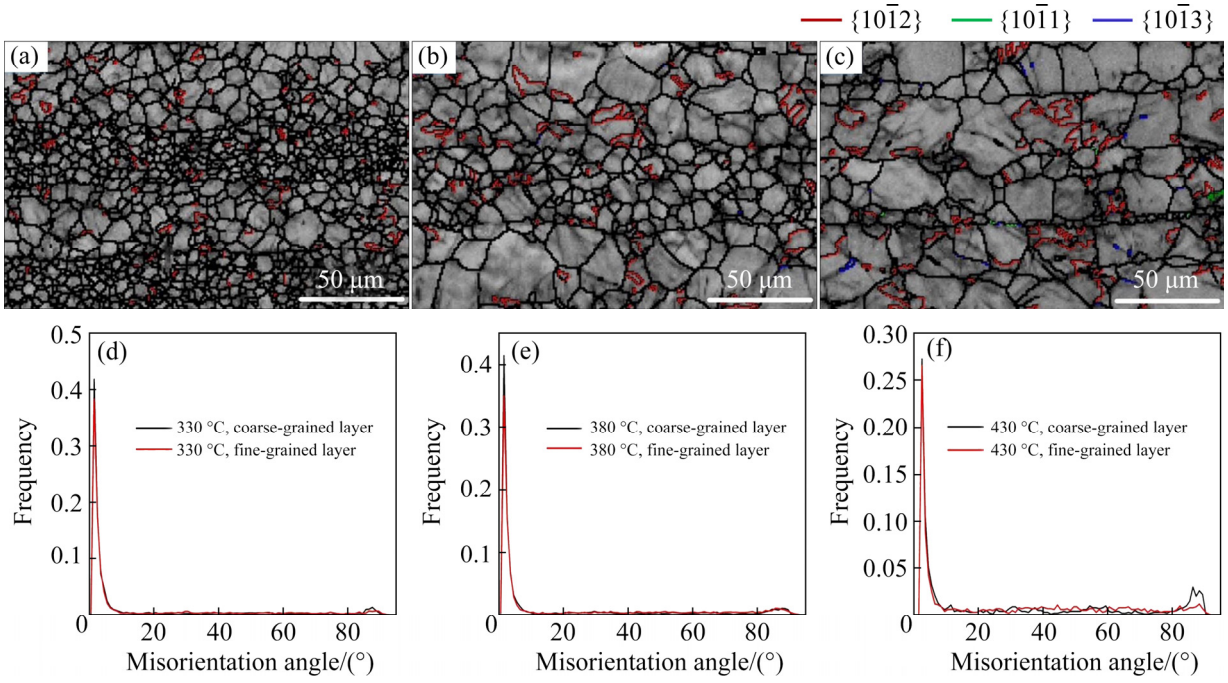

Fig. 11 EBSD observation results of three samples after tensile tests: (a−c) Band contrast maps of samples at extrusion temperatures of 330, 380 and 430 °C, respectively; (d−f) Corresponding misorientation angle distribution maps of (a−c)

The calculated volume fractions of tensile twins in coarse-grained and fine-grained layers of Sample N2 at 330, 380 and 430 °C are 1.7%, 3.7%, 5.0% and 1.2%, 2.2%, 2.6%, respectively. The volume fractions of tensile twins in coarse-grained and fine-grained layers gradually increase. This is due to the increasing grain size at elevated extrusion temperatures. The coordinated plastic strain (ε_{twin}) of the $\{10\bar{1}2\}$ tensile twins can be calculated by Eq. (8) [39]:

$$\varepsilon_{twin}=f_{twin}m_2\gamma_{twin} \quad (8)$$

where f_{twin} is the volume fraction, m_2 is the mean SF, and γ_{twin} is the characteristic shear factor (0.13) [39]. At extrusion temperatures of 330, 380 and 430 °C, the average SF values of tensile twins in coarse- and fine-grained layers of Sample N2 are 0.04, 0.04, 0.05 and 0.12, 0.10, 0.14, respectively. Based on Eq. (8), the total ε_{twin} values of corresponding samples are 0.02%, 0.048% and 0.08%. Although the plastic strain contributed by these tension twins is small, the activated twinning can adjust the orientation of crystals, which relieves the stress concentration to stimulate further slip and maintain large plastic deformation. Meanwhile, the formation of twin boundaries also plays a certain role in the material strengthening.

4.2 Deformation mechanism

IGMA distribution has a great advantage to determine the dominant slip modes as lots of deformed grains rapidly. It is based on the bending of crystal lattice around a certain Taylor axis under the action of slip. The slip modes in a deformed grain can be identified via matching the Taylor axis in Table 3 [40]. By means of the orientation information of EBSD, the microstructure with the orientation between 2.5° and 5° is analyzed, and a precise effect on the qualitative distribution of IGMA can be exerted [41,42].

Figure 12 shows IGMA distributions of Sample N2 at different temperatures. It can be seen that IGMA distributions of Sample N2 at 330 and 430 °C mainly focus on two regions, including the $\langle 0001\rangle$ axis and the $\langle uwt0\rangle$ with the $\langle 01\bar{1}0\rangle - \langle \bar{1}2\bar{1}0\rangle$ arc, which indicates that basal $\langle a\rangle$, prismatic $\langle a\rangle$ and pyramidal $\langle c+a\rangle$ slips are activated. For Sample N2 at 380 °C, IGMA distributions are concentrated along $\langle uwt0\rangle$ with the highest maximum intensity (MI) (2.37) and locate in the $\langle 01\bar{1}0\rangle - \langle \bar{1}2\bar{1}0\rangle$ arc, while a small amount of IGMA distributions around the $\langle 0001\rangle$ axis are observed, implying the existence of a weak in-grain orientation spreads (IGOS). Although the pyramidal $\langle c+a\rangle$ slips are hard to be activated at room temperature due to the high CRSS, the Gd element dramatically changes the c/a axial ratio of hexagonal close-packed structure in Mg alloys and reduces the CRSS of pyramidal $\langle c+a\rangle$ slips. These results demonstrate that basal $\langle a\rangle$ and pyramidal $\langle c+a\rangle$ slips are synergy operative. Moreover, basal $\langle a\rangle$ slips play a dominant role in deformation modes due to the low CRSS. In addition, the effect of prismatic $\langle a\rangle$ slips on plastic deformation decreases.

In order to elucidate the role of different slip modes in coarse-grained and fine-grained layers, IGMA distributions are shown in Fig. 12. Their MI is higher than 2.0 (m.u.d.), which is supposed to develop preferential IGMA [43]. Interestingly, the prismatic $\langle a\rangle$ slips are mainly contributed by fine-grained layers, especially for Sample N2 at 430 °C, while the basal $\langle a\rangle$ and pyramidal $\langle c+a\rangle$ slips are mainly contributed by coarse-grained layers, especially for Sample N2 at 380 °C. The activation of pyramidal $\langle c+a\rangle$ slips also contributes to coordinate further plastic deformation. This activation may also be related to the texture and the change of stress state [11,33−35], which is necessary to further study in future work.

Table 3 Taylor axes corresponding to slip systems observed in Mg alloys

Slip mode	Slip type	Burgers vector	Number of slip system	Taylor axes	Variant
Basal $\langle a\rangle$	$\{0001\}\langle 11\bar{2}0\rangle$	$a/3\langle 11\bar{2}0\rangle$	3	$\langle 1\bar{1}00\rangle$	3
Prismatic $\langle a\rangle$	$\{10\bar{1}0\}\langle 1\bar{2}10\rangle$	$a/3\langle 11\bar{2}0\rangle$	3	$\langle 0001\rangle$	1
Pyramidal $\langle a\rangle$	$\{10\bar{1}1\}\langle 1\bar{2}10\rangle$	$a/3\langle 11\bar{2}0\rangle$	6	$\langle 10\bar{1}\bar{2}\rangle$	6
Pyramidal I $\langle c+a\rangle$	$\{10\bar{1}1\}\langle 11\bar{2}\bar{3}\rangle$	$a/3\langle 11\bar{2}3\rangle$	12	$\langle \bar{2}5\ 41\ \bar{1}69\rangle$	6
Pyramidal II $\langle c+a\rangle$	$\{11\bar{2}2\}\langle 11\bar{2}\bar{3}\rangle$	$a/3\langle 11\bar{2}3\rangle$	6	$\langle \bar{1}100\rangle$	3

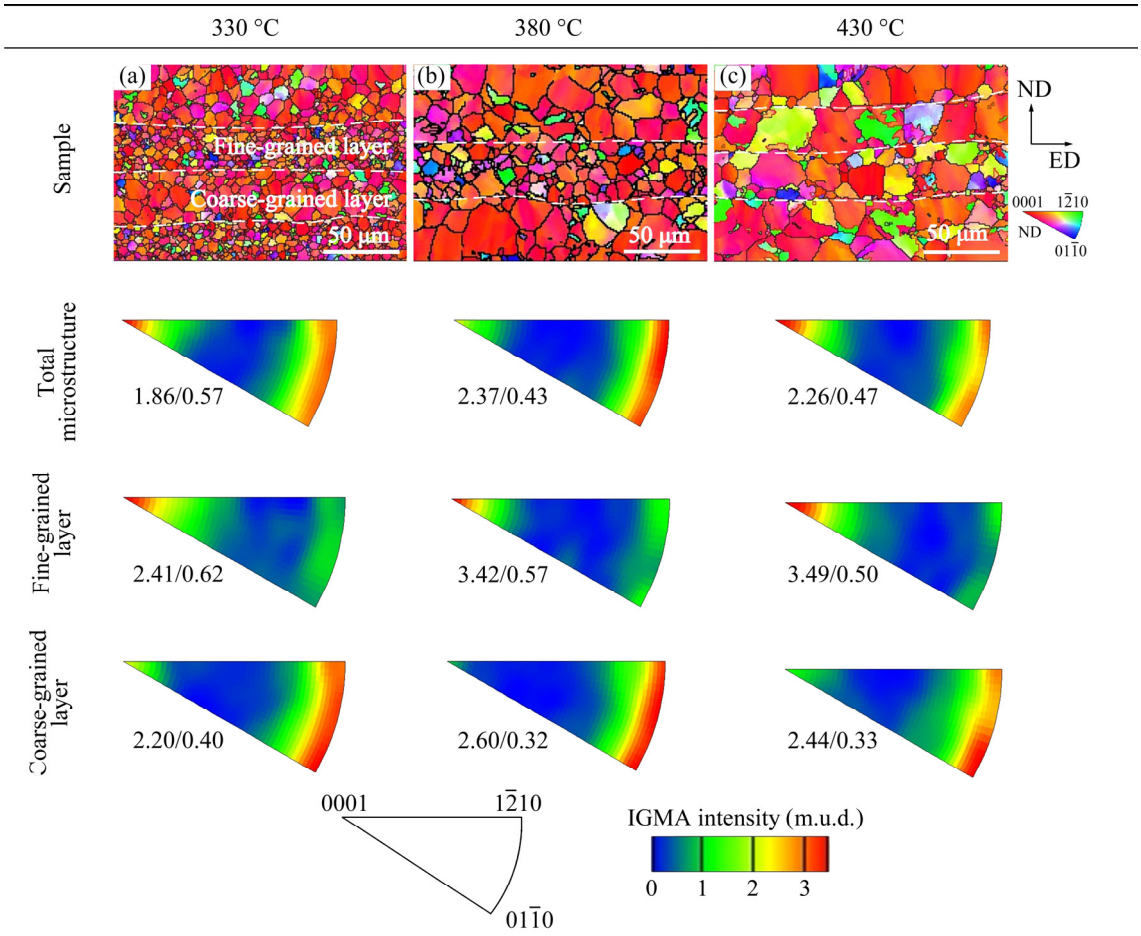

Fig. 12 IPF and corresponding IGMA distributions of Sample N2 at 330 °C (a), 380 °C (b) and 430 °C (c) after tensile tests

5 Conclusions

(1) The grain size difference of Sample N2 has no significant change at 380 °C compared with that at 330 °C, while the grains have grown heavily and nearly present a homogeneous structure at 430 °C. With increasing extrusion temperature, the growth rate of recrystallized grains in fine-grained layers is faster than that in coarse-grained layers. Meanwhile, the precipitates in fine-grained layers gradually increase and coarsen.

(2) Sample N2 has an excellent combination of strength and ductility at 380 °C, which is mainly due to the heterogeneous texture between the coarse-grained and fine-grained layers. In addition, the HDI strengthening and hardening play a significant role in improving the mechanical properties.

(3) Based on IGMA distributions, the fine-grained layers facilitate the activation of prismatic ⟨*a*⟩ slips, while the activation of basal ⟨*a*⟩ and pyramidal ⟨*c*+*a*⟩ slips is mainly due to coarse-grained layers, especially for Sample N2 at 380 °C. The activation of pyramidal ⟨*c*+*a*⟩ slips is conducive to coordinating further plastic deformation.

Acknowledgments

This work was financially supported by the National Natural Science Foundation of China (Nos. 52071035, U1764253).

References

[1] WANG Bo-ning, WANG Feng, WANG Zhi, LIU Zheng, MAO Ping-li. Fabrication of fine-grained, high strength and toughness Mg alloy by extrusion−shearing process [J]. Transactions of Nonferrous Metals Society of China, 2021, 31(3): 666−678.

[2] MA Ying-zhong, WANG De-xin, LI Hong-xiang, YANG Chang-lin, YUAN Fu-song, ZHANG Ji-shan. Microstructure, mechanical properties and corrosion behavior of quaternary Mg−1Zn−0.2Ca−*x*Ag alloy wires applied as degradable anastomotic nails [J]. Transactions of Nonferrous Metals

Society of China, 2021, 31(1): 111−124.

[3] GUI Zhen-zhen, WANG Feng, ZHANG Jun-yi, CHEN De-xin, KANG Zhi-xin. Precipitation behaviors and mechanical properties of a solution-treated Mg−Gd−Nd−Zn−Zr alloy during equal-channel angular pressing process [J]. Journal of Magnesium and Alloys, 2022, 10: 239−248.

[4] MA Zhen-duo, LI Guo, PENG Qiang, PENG Xiao-dong, CHEN Dao-lun, ZHANG Han-zhu, YANG Yan, WEI Guo-bing, XIE Wei-dong. Microstructural evolution and enhanced mechanical properties of Mg−Gd−Y−Zn−Zr alloy via centrifugal casting, ring-rolling and aging [J]. Journal of Magnesium and Alloys, 2022, 10: 119−128.

[5] ZENG Qi, ZHANG Ying-bo, LI Kang-ning, ZHUANG Ye, LI Jia-heng, YUAN Yong, YIN Dong-di. High-ductility fine-grained Mg−1.92Zn−0.34Y alloy fabricated by semisolid and then hot extrusion [J]. Journal of Magnesium and Alloys. doi: 10.1016/j.jma.2021.05.022.

[6] WU Xiao-lei, ZHU Yun-tian. Heterogeneous materials: A new class of materials with unprecedented mechanical properties [J]. Materials Research Letters, 2017, 5(8): 527−532.

[7] ZHU Yun-tian, WU Xiao-lei. Perspective on hetero-deformation induced (HDI) hardening and back stress [J]. Materials Research Letters, 2019, 7(10): 393−398.

[8] JUNG J, PARK S H, YU H, KIM Y M, LEE Y K, YOU B S. Improved mechanical properties of Mg−7.6Al−0.4Zn alloy through aging prior to extrusion [J]. Scripta Materialia, 2014, 93(15): 8−11.

[9] WANG Hui-yuan, YU Zhao-peng, ZHANG Lei, LIU Chun-guo, ZHA Min, WANG Cheng, JIANG Qi-chuan. Achieving high strength and high ductility in magnesium alloy using hard-plate rolling (HPR) process [J]. Scientific Reports, 2015, 5(1): 17100.

[10] GZYL M, ROSOCHOWSKI A, BOCZKAL S, OLEJNIK L. The role of microstructure and texture in controlling mechanical properties of AZ31B magnesium alloy processed by I-ECAP [J]. Materials Science and Engineering A, 2015, 638(2): 20−29.

[11] YAMASAKI M, HASHIMOTO K, HAGIHARA K, KAWAMURA Y. Effect of multimodal microstructure evolution on mechanical properties of Mg−Zn−Y extruded alloy [J]. Acta Materialia, 2011, 59(9): 3646−3658.

[12] HAN Ting-zhuang, HUANG Guang-sheng, DENG Qian-yuan, WANG Guan-gang, JIANG Bin, TANG Ai-tao, ZHU Yun-tian, PAN Fu-sheng. Grain refining and mechanical properties of AZ31 alloy processed by accumulated extrusion bonding [J]. Journal of Alloys and Compounds, 2018, 745: 599−608.

[13] KIM S H, JUNG J G, YOU B S, PARK S H. Microstructure and texture variation with Gd addition in extruded magnesium [J]. Journal of Alloys and Compounds, 2017, 695: 344−350.

[14] WANG Ye, LI Feng, WANG Yu, XIAO Xing-mao. Texture property and weakening mechanism of Mg−3Al−1Zn alloy by interactive alternating forward extrusion [J]. Journal of Magnesium and Alloys. doi: 10.1016/j.jma.2021. 05.007.

[15] SONG Bo, DU Zhi-wen, YANG Qing-shan, GUO Ning, GUO Sheng-feng, YU Jin-cheng, XIN Ren-long. Effect of pre-rolling path on mechanical properties of rolled ZK60 alloys [J]. Transactions of Nonferrous Metals Society of China, 2021, 31(5): 1322−1338.

[16] AGNEW S R, YOO M H, TOME C. Application of texture simulation to understanding mechanical behavior of Mg and solid solution alloys containing Li or Y [J]. Acta Materialia, 2001, 49(20): 4277−4289.

[17] ASGARI H, ODESHI A G, SZPUNAR J A. Grain size dependence of dynamic mechanical behavior of AZ31B magnesium alloy sheet under compressive shock loading [J]. Materials Characterization, 2015, 106: 359−367.

[18] ZHOU Tao, YANG Zhao, HU Dong, FENG Tao, YANG Ming-bo, ZHAI Xiao-bing. Effect of the final rolling speeds on the stretch formability of AZ31 alloy sheet rolled at a high temperature [J]. Journal of Alloys and Compounds, 2015, 650: 436−443.

[19] IMANDOUST A, BARRETT C D, OPPEDAL A L, WHITTINGTON W R, PAUDEL Y, ELKADIRI H E. Nucleation and preferential growth mechanism of recrystallization texture in high purity binary magnesium−rare earth alloys [J]. Acta Materialia, 2017, 138: 27−41.

[20] KOIKE J, KOBAYASHI T, MUKAI T, WATANABE H, SUZUKI M, MARUYAMA K, HIGASHI K. The activity of non-basal slip systems and dynamic recovery at room temperature in fine-grained AZ31B magnesium alloys [J]. Acta Materialia, 2003, 51(7): 2055−2065.

[21] YOSHINAGA H, HORIUCHI R. On the flow stress of α solid solution Mg−Li alloy single crystals [J]. Materials Transactions of the Japan Institute of Metals, 1963, 4(3): 134−141.

[22] SURESH K, RAO K P, PRASAD Y V R K, HORT N, KAINER K U. Study of hot forging behavior of as-cast Mg−3Al−1Zn−2Ca alloy towards optimization of its hot workability [J]. Materials & Design, 2014, 57(5): 697−704.

[23] JIANG Ming-guang, XU Chao, NAKATA T, YAN Hong, CHEN Rong-shi, KAMADO S. Rare earth texture and improved ductility in a Mg−Zn−Gd alloy after high-speed extrusion [J]. Materials Science and Engineering A, 2016, 667: 233−239.

[24] XU S W, MATSUMOTO N, KAMADO S, HONMA T, KOJIMA Y. Dynamic microstructural changes in Mg−9Al−1Zn alloy during hot compression [J]. Scripta Materialia, 2009, 61(3): 249−252.

[25] WATANABE H, TSUTSUI H, MUKAI T, ISHIKAWA K, KOHZU M, HIGASHI K. Grain size control of commercial wrought Mg−Al−Zn alloys utilizing dynamic recrystallization [J]. Materials Transactions, 2001, 42(7): 1200−1205.

[26] XIAO Lei, YANG Guang-yu. Microstructure evolution, mechanical properties and diffusion behaviour of Mg−6Zn−2Gd−0.5 Zr alloy during homogenization [J]. Journal of Materials Science & Technology, 2018, 34(12): 2246−2255.

[27] DAS S K, KANG Y B, HA T K, JUNG I H. Thermodynamic modeling and diffusion kinetic experiments of binary Mg–Gd and Mg–Y systems [J]. Acta Materialia, 2014, 71: 164−175.

[28] HU Ling-fei, GU Qin-fen, LI Qian, ZHANG Jie-yu, WU Guang-xin. Effect of extrusion temperature on microstructure, thermal conductivity and mechanical properties of a Mg−Ce−Zn−Zr alloy [J]. Journal of Alloys and Compounds, 2018, 741: 1222−1228.
[29] ZENGIN H, TUREN Y. Effect of La content and extrusion temperature on microstructure, texture and mechanical properties of Mg−Zn−Zr magnesium alloy [J]. Materials Chemistry and Physics, 2018, 214: 421−430.
[30] MIRONOV S, ONUMA S, SATO Y S, YONEYAMA S, KOKAWA H. Tensile behavior of friction-stir welded AZ31 magnesium alloy [J]. Materials Science and Engineering A, 2017, 679(2): 272−281.
[31] LIU Shuai-shuai, ZHANG Jun-lei, CHEN Xiang, HUANG Guang-sheng, XIA Da-biao, TANG Ai-tao, ZHU Yun-tian, JIANG Bin, PAN Fu-sheng. Improving mechanical properties of heterogeneous Mg−Gd alloy laminate via accumulated extrusion bonding [J]. Materials Science and Engineering A, 2020, 785(21): 139324.
[32] WU Xiao-lei, JIANG Ping, LIU Chen, YUAN Fu-ping, ZHU Yun-tian. Extraordinary strain hardening by gradient structure [J]. Proceedings of the National Academy of Sciences, 2014, 111(20): 7197−7201.
[33] SHI Pei-jian, ZHONG Yun-bo, LI Yi, REN Wei-lin, ZHENG Tian-xiang, SHEN Zhe, YANG Bing, PENG Jian-chao, HU Peng-fei, ZHANG Yong, PETER K L, ZHU Yun-tian. Multistage work hardening assisted by multi-type twinning in ultrafine-grained heterostructural eutectic high-entropy alloys [J]. Materials Today, 2020, 41: 62−71.
[34] BRITTON T B, WILKINSON A J. Stress fields and geometrically necessary dislocation density distributions near the head of a blocked slip band [J]. Acta Materialia, 2012, 60(16): 5773−5782.
[35] YANG Mu-xin, PAN Yue, YUAN Fu-ping, ZHU Yun-tian, WU Xiao-lei. Back stress strengthening and strain hardening in gradient structure [J]. Materials Research Letters, 2016, 4(3): 145−151.
[36] WU Jia-lin, JIN Li, DONG Jie, WANG Feng-hua, DONG Shuai. The texture and its optimization in magnesium alloy [J]. Journal of Materials Science & Technology, 2020, 42(7): 175−189.
[37] BOHLEN J, NURNBERG M R, SENN J M, LETZIG D, AGNEW S R. The texture and anisotropy of magnesium−zinc−rare earth alloy sheets [J]. Acta Materialia, 2007, 55(6): 2101−2112.
[38] BARNETT M R, KESHAVARZ Z, BEER A G, ATWELL D. Influence of grain size on the compressive deformation of wrought Mg−3Al−1Zn [J]. Acta Materialia, 2004, 52(17): 5093−5103.
[39] SONG Bo, YANG Qing-shan, ZHOU Tao, CHAI Lin-jiang, GUO Ning, LIU Ting-ting, GUO Sheng-feng, XIN Ren-long. Texture control by $\{10\bar{1}2\}$ twinning to improve the formability of Mg alloys: A review [J]. Journal of Materials Science & Technology, 2019, 35(10): 2269−2282.
[40] HADORN J P, HANTZSCHE K, YI J, BOHLEN D, LETZIG J A. Role of solute in the texture modification during hot deformation of Mg−rare earth alloys [J]. Metallurgical and Materials Transactions A, 2012, 43(4): 1347−1362.
[41] SUH B C, KIM J H, BAE J H, HWANG J H, SHIM M S, KIM N J. Effect of Sn addition on the microstructure and deformation behavior of Mg−3Al alloy [J]. Acta Materialia, 2017, 124: 268−279.
[42] CHAUDRY U M, KIM Y S, HAMAD K. Effect of Ca addition on the room-temperature formability of AZ31 magnesium alloy [J]. Materials Letters, 2019, 238: 305−308.
[43] CHUN Y B, BATTAINI M, DAVIES C H J, HWANG S K. Distribution characteristics of in-grain misorientation axes in cold-rolled commercially pure titanium and their correlation with active slip modes [J]. Metallurgical and Materials Transactions A, 2010, 41(13): 3473−3487.

挤压温度对累积挤压工艺制备的异质结构 Mg−Gd 合金复合板组织演化和力学性能的影响

刘帅帅[1,2]，刘 晗[1,2]，张宝煊[1,2]，黄光胜[1,2]，陈 祥[1,2]，汤爱涛[1,2]，蒋 斌[1,2]，潘复生[1,2]

1. 重庆大学 材料科学与工程学院 机械传动国家重点实验室，重庆 400044；
2. 重庆大学 国家镁合金工程研究中心，重庆 400044

摘 要：研究挤压温度对累积挤压工艺制备的异质结构 Mg−1Gd/Mg−13Gd 复合板显微组织和力学性能的影响。结果表明，当挤压温度为 330 ℃时，Mg−1Gd/Mg−13Gd 复合板在连续层之间形成明显的晶粒尺寸差异，随着挤压温度从 380 ℃增加到 430 ℃时，这种差异逐渐消失。此外，细晶层中再结晶晶粒的生长速度快于粗晶层。而且，Gd 元素的扩散能力随着挤压温度的升高而增强，促进细晶层中析出相的增加和粗化。拉伸测试表明，380 ℃下的挤压试样具有优异的强度和塑性结合。这主要归因于粗、细晶层之间的不均匀织构、形变诱导强化和硬化的协同作用。细晶层有利于柱面⟨*a*⟩滑移的激活，而粗晶层有利于基面⟨*a*⟩和锥面⟨*c*+*a*⟩滑移的激活，尤其是在 380 ℃时更为显著。锥面⟨*c*+*a*⟩滑移的激活有助于协调进一步的塑性变形。

关键词：Mg−Gd 合金；异质结构；织构；力学性能；滑移机制

(Edited by Wei-ping CHEN)